

CHIPS-FF: Evaluating Universal Machine Learning Force Fields for Material Properties

Daniel Wines* and Kamal Choudhary

*Material Measurement Laboratory, National Institute of Standards and Technology,
Gaithersburg, MD 20899, USA*

E-mail: daniel.wines@nist.gov

Abstract

In this work, we introduce CHIPS-FF (Computational High-Performance Infrastructure for Predictive Simulation-based Force Fields), a universal, open-source benchmarking platform for machine learning force fields (MLFFs). This platform provides robust evaluation beyond conventional metrics such as energy, focusing on complex properties including elastic constants, phonon spectra, defect formation energies, surface energies, and interfacial and amorphous phase properties. Utilizing 16 graph-based MLFF models including ALIGNN-FF, CHGNet, MatGL, MACE, SevenNet, ORB, MatterSim and OMat24, the CHIPS-FF workflow integrates the Atomic Simulation Environment (ASE) with JARVIS-Tools to facilitate automated high-throughput simulations. Our framework is tested on a set of 104 materials, including metals, semiconductors and insulators representative of those used in semiconductor components, with each MLFF evaluated for convergence, accuracy, and computational cost. Additionally, we evaluate the force-prediction accuracy of these models for close to 2 million atomic structures. By offering a streamlined, flexible benchmarking infrastructure, CHIPS-FF aims to guide the development and deployment of MLFFs for real-world semiconductor

applications, bridging the gap between quantum mechanical simulations and large-scale device modeling.

Keywords: Machine learning force field; deep learning; foundational models; density functional theory; high-throughput; materials discovery; semiconductors

Multiscale modeling in materials science^{1,2} is an essential tool to bridge the gap between atomistic properties, device performance, and manufacturing. With the passage of the U.S. Creating Helpful Incentives to Produce Semiconductors (CHIPS) and Science Act in 2022,³ there has been a renewed focus on modeling semiconductor materials, devices, and components. Various approaches to semiconductor modeling can be applied at different scales, including quantum mechanical tools such as density functional theory (DFT),⁴ classical atomistic simulations such as molecular dynamics (MD),⁵ technology computer-aided design (TCAD)⁶ and various machine learning (ML) models.⁷⁻¹³

In order to better inform semiconductor device models, accurate structure-to-property relationships must be established, which often require more computationally expensive quantum mechanical approaches. Accurate structural relaxations of defect structures and semiconductor interfaces are key to uncovering the underlying physics that govern device performance. For example, defects in semiconductors can introduce energy levels within the band gap, which can impact carrier mobility and concentration and create traps, leading to non-radiative recombination of holes and electrons.¹⁴⁻¹⁹ Semiconductor surfaces and interfaces are especially important to consider since they are the building blocks of devices, impacting charge carrier behavior (band alignment), electrical properties (i.e., Schottky vs. Ohmic), thermal management and device efficiency.²⁰⁻²⁵ In addition, the combination of semiconductor materials and high-dielectric amorphous structures are essential for building Metal-Oxide-Semiconductor Field-Effect Transistors (MOSFETs).²⁶⁻³¹

Due to the costly scaling of DFT (N^3 , where N is the number of electrons), high-throughput calculations of larger simulation cells required to study defects, surfaces and interfaces are not feasible. Unfortunately, many of the current classical atomistic interatomic

potentials do not have the capability to achieve near-DFT accuracy and capture these complex interactions. In addition, most classical potentials are limited in their transferability to various systems and experimental conditions. Early attempts to create a universal force field for the entire periodic table were limited in their accuracy.³² For this reason, many researchers have explored machine learning force fields (MLFFs) trained on highly-accurate DFT calculations as a viable route to bridge the gap between quantum mechanical accuracy and large-scale atomistic simulations.

One of the pioneering MLFF architectures was developed by Behler and Parrinello in 2007 using neural networks.³³ Other MLFF methods include Gaussian processes-based Gaussian approximation potentials (GAP),³⁴ spectral neighbor analysis potential (SNAP)³⁵ and Allegro.³⁶ Graph neural network (GNN)-based machine learning force fields (MLFFs) are now considered state-of-the-art due to their superior accuracy and transferability. With the public availability of large DFT databases (such as the Materials Project,³⁷ JARVIS-DFT,^{38,39} OQMD,^{40,41} and Alexandria⁴²⁻⁴⁵), several researchers have trained GNN force fields on full DFT databases, encompassing the entire periodic table. These so-called universal/unified/foundational machine learning force fields (uMLFFs) have been successful at reproducing near-DFT accuracy for a wide-range of systems.

A major advantage of utilizing these pretrained uMLFF architectures is that expensive DFT dataset generation is not an initial requirement. These pretrained uMLFFs can be used in place of DFT or fine tuned on more tailored datasets or tasks. Such uMLFFs have shown remarkable potential for numerous applications including modeling of defects and surfaces,^{46,47} disordered alloys,⁴⁸ high-pressure superconductors,⁴⁹ solid-solution energetics and ion migration barriers,⁴⁶ catalysis,⁵⁰ thermal conductivity,⁵¹ semiconductor interfaces,²¹ guiding inverse materials design^{12,52,53} and many other applications in chemistry, physics and materials science.⁵⁴⁻⁵⁶ Important quantities such as optimized structure, elastic properties, vibrational properties (phonons), stability, thermal properties, defect formation energy and surface energy can be easily computed from uMLFFs at a significantly lower

cost than DFT. Additionally, uMLFF structural relaxations of bulk semiconductors, point defects, surfaces and interfaces can be coupled with other low-cost tools (direct prediction with GNNs,^{17,17,21,57,58} tight binding^{59,60}) to predict electronic properties. uMLFFs can also be used to perform structure searches (replacing hundreds to tens of thousands of DFT relaxation calculations), which can be followed by a single DFT calculation for electronic properties of the target structure.

One of the first graph-based uMLFF architectures introduced in 2022 was M3GNet from Chen and Ong.⁶¹ M3GNet has since transformed into MatGL (Materials Graph Library),⁶² a re-implementation of M3GNet built on the Deep Graph Library (DGL)⁶³ and PyTorch.⁶⁴ M3GNet evolved from the MEGNet (MatERials Graph Network) property prediction model introduced in Ref.⁶⁵ M3GNet was trained on $\approx 60,000$ inorganic materials ($\approx 190,000$ relaxation steps) in the Materials Project (MP), covering 89 elements of the periodic table.⁶¹ This dataset is commonly referred to as MPF.⁶¹ In M3GNet, the angles (representing three-body interactions) are incorporated by aggregating to bonded atoms within the graph convolution steps to update atoms, bonds and properties.⁶¹ The Atomistic Line Graph Neural Network (ALIGNN)-FF model⁶⁶ was introduced in 2022 and was trained on the JARVIS-DFT dataset of $\approx 75,000$ materials ($\approx 300,000$ relaxation steps, ALIGNN-FF DB). ALIGNN-FF evolved from the ALIGNN property prediction model released in 2021.⁵⁸ The ALIGNN model achieved significant improvement in property prediction tasks due to the inclusion of bond-angles in terms of line graphs, which previous GNN models lacked.⁵⁸ The earlier versions of ALIGNN-FF utilized a k-nearest neighbor graph,⁶⁶ while the updated version of ALIGNN-FF (2024.12.2) utilizes a radius graph, making it faster and more robust. Another uMLFF that utilizes a crystal graph (atom graph and bond graph) is the Crystal Hamiltonian Graph Neural Network (CHGNet),⁶⁷ which was proposed in 2023. This model was trained on the Materials Project Trajectory (MPtrj) dataset,⁶⁷ which includes DFT calculations for $\approx 150,000$ materials (≈ 1.58 million relaxation steps). CHGNet also incorporates magnetic moments into the training process to enhance the description of chemical reactions.⁶⁷

MACE,^{54,68,69} an equivariant message passing neural network potential, uses higher order messages (higher than two body) combined with atomic cluster expansion (ACE),^{70,71} which is a method for deriving an efficient body-ordered symmetric polynomial basis to represent functions of atomic neighborhoods. A pre-trained model for the entire periodic table (trained on MPTrj) for MACE was released in late 2023⁵⁴ (referred to as MACE-MP-0). In late 2024, a new pretrained version of MACE (known as MACE-MPA-0) was released, which is trained on a combination of MPTrj and Alexandria.⁷² SevenNet (Scalable EquiVariance Enabled Neural Network),⁷³ another equivariant message passing uMLFF, is based on the NequIP⁷⁴ architecture for building E(3)-equivariant force fields. SevenNet trained on the MPtrj dataset and was released in 2024. In addition to these open source models, there have been proprietary uMLFF models developed including MatterSim (Microsoft)⁷⁵ and GNoME (Google DeepMind).⁷⁶ A version of MatterSim (MatterSim-v1), which has a similar but slightly modified architecture to M3GNet and is trained on over 17 million structures sampled from Materials Project, Alexandria, and Microsoft’s own dataset (consisting of additional structures and MD trajectories at ambient and extreme conditions), was made open source to the community in December 2024.⁷⁷ The Orb⁷⁸ pretrained uMLFF, released in fall 2024, was developed by the startup company Orbital Materials, where superior performance for force and energy predictions were demonstrated at significantly reduced computational cost.^{55,79,80} Orb utilizes an attention augmented Graph Network-based Simulator (GNS),⁸¹ which is a type of Message Passing Neural Network (MPNN).⁸² In contrast to equivariant models such as MACE and SevenNet, Orb does not utilize equivariant message passing. The open source Orb model (orb-v2) is trained on MPtrj and Alexandria (over 3 million materials and 32 million relaxation steps).⁵⁵ In late 2024, Meta FAIR Chemistry released the Open Materials 2024 (OMat24)⁸³ models and dataset, which contains over 110 million DFT calculations and pretrained uMLFF models based on the EquiformerV2⁸⁴ architecture, which is a highly accurate equivariant transformer model. OMat24 offers various sized models trained on OMat, MPTrj and Alexandria.

Recently, interest in the field of uMLFFs has grown immensely (from academia, government and industry), as seen by the several models above and various use cases of new model architectures. Given the current state of the field, benchmarking the performance of uMLFFs is imperative. Large-scale efforts to benchmark the performance of various pretrained uMLFF architectures have emerged such as Matbench Discovery^{80,85} and the JARVIS-Leaderboard,^{86,87} which calculate error metrics and allow for new models to be uploaded as time progresses. There have been focused benchmarking efforts for more involved properties beyond energy. Yu et al.⁸⁸ performed a systematic assessment of uMLFFs (M3GNet, ALIGNN-FF, CHGNet and MACE), calculating properties such as optimized structure, formation energy, bulk modulus, and phonon band structure, comparing directly to DFT to calculate error metrics. Benchmarking of more advanced properties such as surface energies, defect formation energies, solid-solution energetics, and ion migration barriers have recently been performed with M3GNet, CHGNet and MACE.^{46,47} In addition, a high-level assessment of uMLFF computed thermal conductivity has been conducted with M3GNet, CHGNet, MACE, SevenNet and ORB by Poła et al.⁵¹ More recently, Zhu et al. utilized M3GNet, CHGNet, MACE, SevenNet, and ORB to accelerate the prediction of CALPHAD-based phase diagrams for complex alloys⁸⁹ and Lowe et al. performed in-depth benchmarking of phonons for over 10,000 materials using all of the recent state-of-the-art uMLFFs.⁹⁰ These recent efforts have highlighted the successes and limitations of various uMLFF architectures, and have emphasized the need for a comprehensive publicly available benchmarking platform. Such a platform allows the community to make informed decisions on regarding uMLFFs, outweighing factors such as computational cost versus accuracy. In addition, researchers may find systematic trends in the uMLFF results which can help others to understand the applicability of each uMLFF type. Well-understood systematic trends in DFT functionals (i.e., the underbinding and lattice constant errors of GGA) have been exploited to identify new exfoliable van der Waals (vdW) materials.⁹¹ In contrast to the Jacob’s Ladder metaphor of DFT exchange-correlation functionals,⁹² where the “rungs” of

the ladder refer to the increasing complexity (and computational cost) and accuracy of the functionals, there (as of yet) exists no systematic assessment or generalizable statements for uMLFFs. As uMLFFs begin to replace DFT calculations, such analysis is needed to help the community better develop new force fields or fine-tune existing force fields for downstream applications.

In this work, we present CHIPS-FF (Computational High-performance Infrastructure for Predictive Simulation-based Force Fields): a generalized user-friendly open-source benchmarking package to test various uMLFFs for a number of properties beyond energy. We have implemented a streamlined workflow to use uMLFFs for structural relaxation, bulk modulus, elastic properties, point defect formation energy, surface energy, interfacial properties (work of adhesion), molecular dynamics and creation of amorphous structures, all with automated error metrics from JARVIS-DFT. In contrast to large scale benchmarking efforts such as Matbench Discovery,^{80,85} which requires users to submit contributions covering enormous test sets (on the order of 200,000), CHIPS-FF allows for robust benchmarking on smaller datasets and more complex properties. Although our framework is agnostic to the type of material, we chose a set of 104 materials that are most relevant for semiconductor devices as a case study. Additionally, we evaluate force-prediction accuracy of these models for close to 2 million atomic structures from Materials Project and JARVIS-DFT databases. We intend this codebase and benchmarking dataset to benefit the MLFF community and aid in the development of future models.

The CHIPS-FF workflow mainly utilizes the Atomic Simulation Environment (ASE)⁹³ and JARVIS-Tools^{38,39} to perform atomistic simulations in Python. In terms of pretrained uMLFF models, we utilized ALIGNN-FF: 2.12.2024 (trained on 307k entries from JARVIS-DFT), CHGNet: 0.3.8, , MatGL: 1.1.2 (using both the M3GNet-MP-2021.2.8-PES and M3GNet-MP-2021.2.8-DIRECT-PES⁹⁴ models), MACE: 0.3.10 (using MACE-MP-0 and MACE-MPA-0), SevenNet-0: 0.9.2 (using the 11July2024 model), orb-models: 0.4.1 (orb-v2 and orb-d3-v2, which utilizes the D3 dispersion correction⁹⁵), and MatterSim-v1 (MatterSim-

v1.0.0-5M). In addition, we benchmarked a MACE force field trained on the newly released Alexandria dataset presented in Ref. ⁴⁵ (this model was trained on over 200,000 2D material calculations with the PBEsol⁹⁶ functional and is referred to as MACE^{2D} in that work⁹⁷). In our work, we refer to this model as mace-alexandria (which is distinct from mace-mpa). For the OMat24 models from Meta, we tested the three EquiformerV2 (eqV2) models trained on OMat (Small: 31M (million), medium: 86M, and large: 153M in terms of model parameters) and two eqV2 models trained on OMat+MPTrj+Alexandria (Small: 31M and medium: 86M).^{56,83} These models are named as: eqV2_31M_omat, eqV2_86M_omat, eqV2_153M_omat, eqV2_31M_omat_mp_salex, and eqV2_86M_omat_mp_salex.^{56,83}

Initial structures were obtained from the JARVIS-DFT database (but not limited by it) and then optimized using the FIRE⁹⁸ algorithm within ASE. For bulk relaxations, atomic coordinates and lattice vectors were allowed to relax, but for surfaces and vacancy calculations, cell volume was fixed and atomic positions were allowed to relax. The maximum force value (stopping criterion for relaxation) was set to 0.05 eV/Å. If a calculation did not reach the stopping criterion by 200 steps, it was considered unconverged. If a structure did not reach convergence within 200 steps, the final structure and energy at 200 steps was logged and used for subsequent portions of the workflow. The bulk modulus was obtained by applying isotropic strain to the system from -6 % to +6 % and using a Murnaghan fit for the equation of state. The elastic tensor was computed using the Elastic package.⁹⁹⁻¹⁰¹ For bulk modulus and elastic tensor calculations, the conventional cell was used. We utilized the phonopy^{102,103} package to perform simulations of the phonon spectrum using the finite displacement method,¹⁰⁴ where a 2 x 2 x 2 supercell was constructed from the initial unit cell and a displacement of 0.2 Å was used. From these phonopy results, we also extracted the Helmholtz free energy (and zero point energy at 0 K), entropy and heat capacity as a function of temperature. We have added capabilities to CHIPS-FF to compute the thermal expansion of each material at constant pressure and the lattice thermal conductivity, utilizing the quasi-harmonic approximation¹⁰⁵ implemented in phonopy and phono3py^{102,103}

respectively (these simulations are ongoing and will be discussed in future work). JARVIS-Tools was used to automatically generate supercells for neutral point defects (vacancies) and non-polar surfaces (both of which were later relaxed with uMLFFs). Defect supercells are constructed from the conventional cell and enforced to have a lattice vector c as close to 8 Å as possible, where single vacancies are created based on Wyckoff-position information for each atomic species in the crystal. The following formula is used to obtain the vacancy formation energy (E_{vac}):

$$E_{\text{vac}} = E_{\text{defect}} - E_{\text{bulk}} + \mu \tag{1}$$

where E_{defect} is the total energy of the defect supercell, E_{bulk} is the energy of the bulk structure (no defect) and μ is the chemical potential of the missing atom. The lowest energy crystal structure of the elemental solid (from JARVIS-DFT) is used to calculate the chemical potential with each respective uMLFF (where the structure is fully re-relaxed). Surfaces were generated for miller indices of [1, 0, 0], [1, 1, 1], [1, 1, 0], [0, 1, 1], [0, 0, 1], and [0, 1, 0], skipping any polar surfaces in the surface relaxation. Each surface contained at least 4 layers and 18 Å of vacuum. The surface energy of each non-polar surface was calculated as:

$$\gamma = \frac{E_{\text{surface}} - N \cdot E_{\text{bulk}}}{2A} \tag{2}$$

where E_{surface} is the energy of the surface structure, E_{bulk} is the energy of the bulk structure, N is the number of bulk unit cells in the surface, and A is the cross sectional area of the surface. In order to study amorphous materials, we have implemented finite-temperature molecular dynamics into our workflow to perform melt/quench simulations using Berendsen NVT (Number of particles, Volume, Temperature ensemble) dynamics within ASE. For our case study of amorphous Si, we used a timestep of 1 femtosecond and ran the simulation at 3500 K for 10 ps (melt) and 300 K for 20 ps (quench). For benchmarking calculations to compare uMLFF results to, we performed similar ab initio MD (AIMD) calculations with

the Vienna Ab initio Simulation Package (VASP) code, using projector augmented wave (PAW) pseudopotentials^{106,107} and the vdW-DF-optB88 functional. In order to perform calculations for material interfaces, we utilized InterMat,²¹ a newly developed package for the generation and calculation of interface structures (substrate plus film). The initial interface is obtained by creating a superlattice or alternating slab junction (ASJ) structure (without vacuum padding)^{108,109} and then using the Zur algorithm¹¹⁰ to obtain the best candidate interface. From here, we computed the relative alignment between the film and substrate in the in-plane (xy) direction by performing a grid search with a 0.05 fractional spacing interval with each respective uMLFF model. In addition to determining the optimal in-plane orientation between the substrate and film, this gives us a qualitative estimate of how smooth the potential energy surface is at the interface for each pretrained uMLFF. From this calculation, we also determined the work of adhesion (W_{ad}) at the interface with:

$$W_{\text{ad}} = \gamma_{\text{film}} + \gamma_{\text{substrate}} - \gamma_{\text{interface}} \quad (3)$$

where γ_{film} is the surface energy of the film, $\gamma_{\text{substrate}}$ is the surface energy of the substrate and $\gamma_{\text{interface}}$ is the interfacial energy calculated as:

$$\gamma_{\text{interface}} = \frac{E_{\text{interface}} - E_{\text{film}} - E_{\text{substrate}}}{A} \quad (4)$$

where $E_{\text{interface}}$ is the total energy of the interface, E_{film} is the total energy of the film, $E_{\text{substrate}}$ is the total energy of the substrate and A is the cross sectional area.

A majority of the reference data used to compare our uMLFF results to were obtained from the JARVIS-DFT database, which contains relaxed structural data (primitive lattice vectors, volume), elastic properties (bulk modulus, elastic tensor) and phonon band structure.^{38,39} Within JARVIS-DFT, there exists a database of single vacancy calculations¹⁶ and surfaces²¹ that were both used for benchmarking these uMLFFs. All of the DFT data in JARVIS was computed with the vdW-DF-optB88¹¹¹ functional, which is a modified Gen-

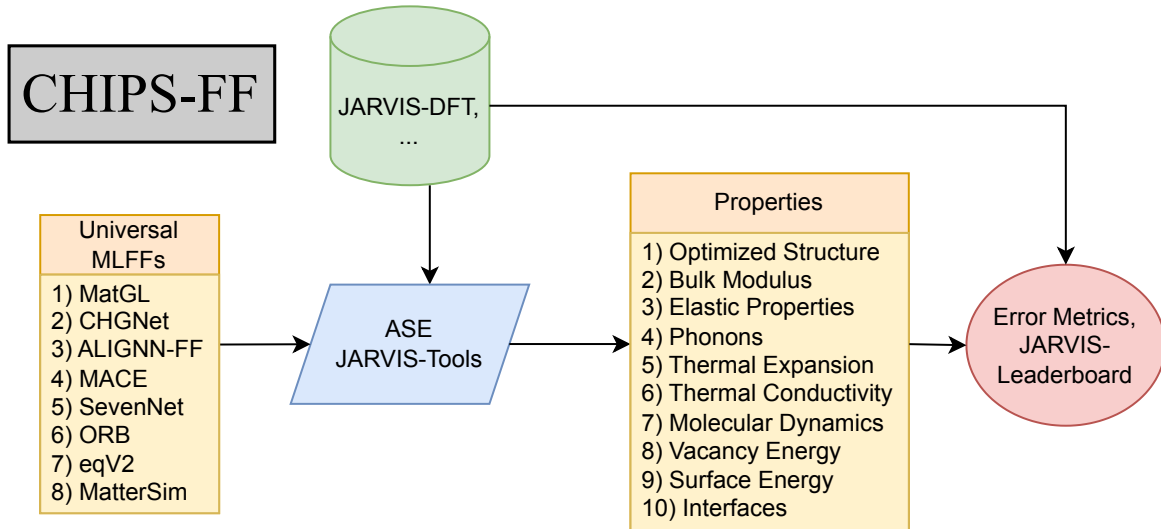


Figure 1: A full schematic of the CHIPS-FF workflow.

eralized Gradient Approximation (GGA) functional designed to explicitly include van der Waals (vdW) interactions. This is slightly different than other materials repositories such as the Materials Project (MPtrj), which mostly contains DFT calculations performed with the Perdew Burke Ernzerhof (PBE)¹¹² GGA functional. Despite mostly comparing to JARVIS-DFT results (vdW-DF-optB88), the CHIPS-FF workflow has a flexible framework to use any DFT dataset as a ground truth (i.e., the Materials Project, Alexandria, a users own DFT dataset, etc.). In addition, the platform is flexible enough to compare uMLFF results directly to available experimental values.

Fig. 1 depicts a full schematic of the CHIPS-FF workflow. In this workflow, initial structures are taken from the JARVIS-DFT database. JARVIS-Tools is used to pull structures from the JARVIS-DFT database and generate supercell surface and defect structures prior to atomistic simulations. Various uMLFF calculators are accessed through ASE. So far, we have implemented MatGL, CHGNet, ALIGNN-FF, MACE, SevenNet, ORB, MatterSim, and eqV2 (OMat24). As new pretrained force fields are developed over time, they will be added to the workflow. In addition, CHIPS-FF offers the flexibility for the user to add their own force field or property to the pipeline. Once each uMLFF is loaded and run

Table 1: The percentage of unconverged structural relaxations for bulk, surface, and vacancy calculations for each uMLFF. The green highlights which models have the highest convergence rate.

uMLFF Type	Bulk	Surface	Vacancy
alignn_ff	6.7	37.5	39.6
chgnet	0.0	1.1	6.2
eqV2_153M_omat	0.0	14.8	31.2
eqV2_31M_omat	0.0	17.0	25.0
eqV2_31M_omat_mp_salex	0.0	5.7	0.0
eqV2_86M_omat	1.9	18.2	27.1
eqV2_86M_omat_mp_salex	0.0	5.7	2.1
mace	0.0	6.8	25.0
mace-alexandria	2.9	15.9	33.3
mace-mpa	0.0	6.8	33.3
matgl	0.0	4.5	14.6
matgl-direct	3.8	6.8	12.5
mattersim	0.0	4.5	16.7
orb-d3-v2	0.0	1.1	2.1
orb-v2	1.0	0.0	0.0
sevensnet	0.0	2.3	41.7

Table 2: The mean absolute error (MAE) and total computational time for a variety of material properties calculated with each uMLFF type. The MAE is calculated with respect to JARVIS-DFT data. Properties include (in order) lattice constants a, b, c, volume, bulk modulus, C11 and C44 components of the elastic tensor, and phonon band structure. The computational time is measured per CPU. An interactive and up-to-date version of the table is available in the JARVIS-Leaderboard.

uMLFF Type	err_a Å	err_b Å	err_c Å	err_vol Å ³	err_kv GPa	err_c11 GPa	err_c44 GPa	err_phonon cm ⁻¹	Time seconds
alignn_ff	0.087	0.102	0.137	9.95	122	196	74	150	8.8 x 10 ⁴
chgnet	0.046	0.049	0.109	3.58	85	59	45	68	3.5 x 10 ⁴
eqV2_153M_omat	0.036	0.040	0.111	2.90	117	70	32	49	1.6 x 10 ²
eqV2_31M_omat	0.029	0.032	0.099	3.05	115	78	37	48	3.4 x 10 ⁵
eqV2_31M_omat_mp_salex	0.028	0.030	0.096	3.17	112	47	41	48	2.7 x 10 ⁵
eqV2_86M_omat	0.033	0.040	0.094	3.41	116	85	35	49	9.7 x 10 ⁵
eqV2_86M_omat_mp_salex	0.027	0.030	0.100	3.14	114	45	35	48	7.2 x 10 ⁵
mace	0.035	0.038	0.084	3.00	94	43	38	58	7.2 x 10 ⁴
mace-alexandria	0.081	0.086	0.206	6.05	76	96	45	81	2.5 x 10 ⁵
mace-mpa	0.044	0.046	0.098	3.57	110	35	34	49	8.4 x 10 ⁴
matgl	0.052	0.057	0.128	3.50	83	64	41	78	1.7 x 10 ⁴
matgl-direct	0.044	0.046	0.106	2.88	84	73	50	85	2.5 x 10 ⁴
mattersim	0.031	0.033	0.110	3.18	110	32	32	48	5.9 x 10 ⁴
orb-d3-v2	0.031	0.030	0.048	1.90	130	74	74	52	2.7 x 10 ⁴
orb-v2	0.023	0.025	0.159	3.38	119	80	74	49	2.4 x 10 ⁴
sevensnet	0.035	0.038	0.100	3.43	103	46	37	53	5.7 x 10 ⁴

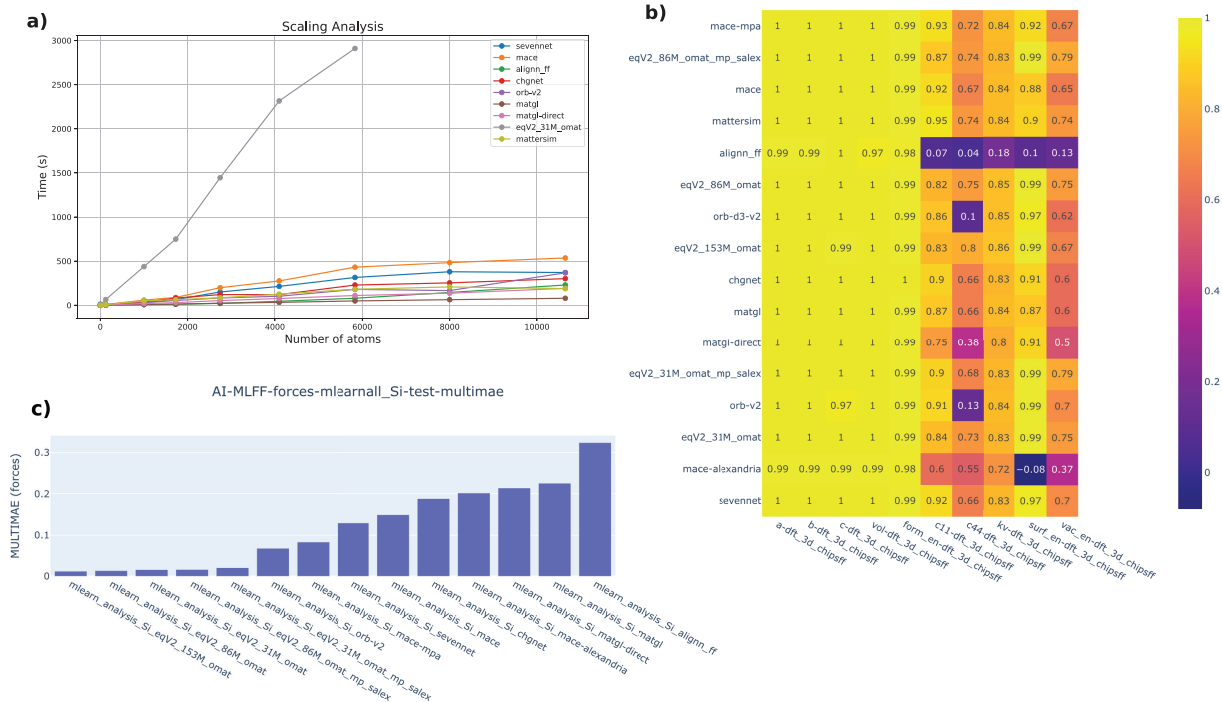


Figure 2: a) Scaling analysis of various uMLFF up to 10,000 atoms (for a supercell of Cu), b) an example JARVIS-Leaderboard entry for the force MAE of the MLEARN dataset, c) an example of the interactive error metrics within the JARVIS-Leaderboard (Pearson correlation coefficient).

through the ASE calculator, a variety of properties can be computed including: optimized structure, bulk modulus (equation of state fitting), elastic tensor (elastic package), phonons (phonopy), thermal expansion (phonopy), thermal conductivity (phono3py), molecular dynamics, vacancy formation energy, surface energy, and interface properties (InterMat). As these calculations are carried out, detailed logging information is saved, including the computational timing for each stage of the calculation and whether or not each stage converged. Once these material properties are computed with each uMLFF, they are cross checked with entries in the JARVIS-DFT database and the mean absolute error (MAE) for each property is computed. For spectral quantities such as the phonon band structure, we computed the MAE for each band along the q-point path using:

$$\text{MAE} = \frac{1}{N_q} \sum_{q\nu} |\omega_{q\nu}^{\text{uMLFF}} - \omega_{q\nu}^{\text{DFT}}| \quad (5)$$

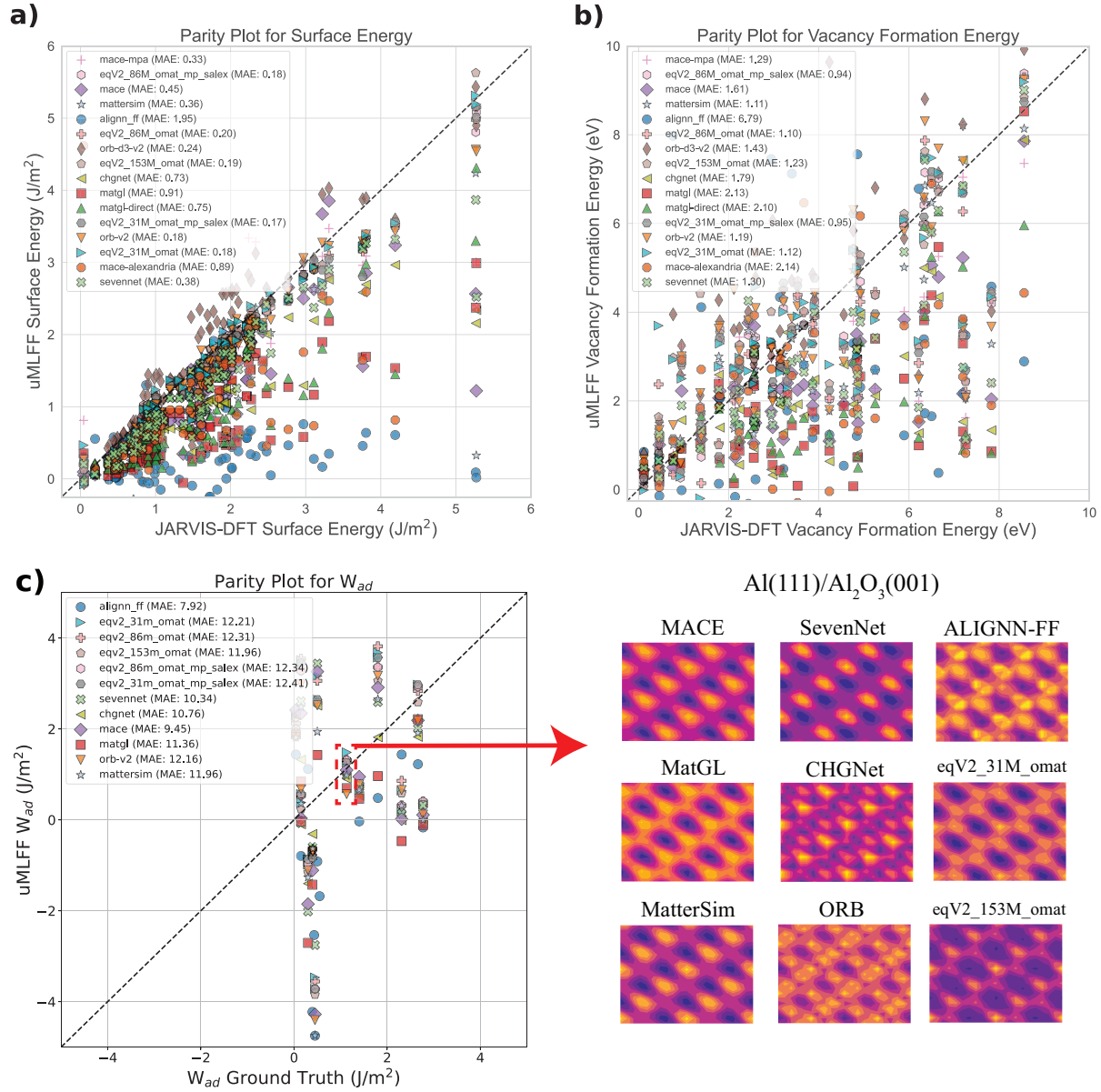


Figure 3: Parity plots for a) surface energy (in J/m^2) and b) vacancy formation energy (in eV) for each uMLFF type with respect to JARVIS-DFT data (MAE is given in the inset). c) Depicts the parity plot for work of adhesion (W_{ad} in J/m^2) for several material interfaces and MAE with respect to previous calculated and experimental data (taken from Ref. ¹¹³). To the right of the parity plot, we focus on the best performing W_{ad} prediction for the Al(111)Al₂O₃(001) interface, showing the xy grid search and optimal in-plane interface configurations with each uMLFF.

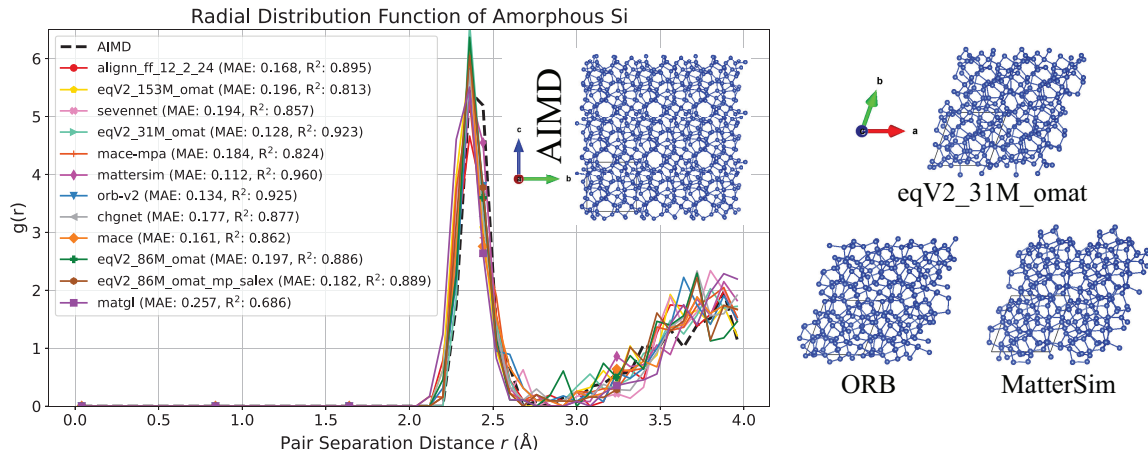


Figure 4: The calculated radial distribution function ($g(r)$) as a function of pair separation distance computed with several uMLFF models for amorphous Si (by performing melt/quench simulations). Ab initio (AIMD) results are given as a ground truth benchmark (black dotted line) and the MAE and R^2 with respect to AIMD is reported in the inset. The atomic structure for amorphous Si is given for AIMD and the best performing uMLFF models (MatterSim, eqV2_31M_omat and ORB).

where $\omega_{q\nu}$ is the phonon energy (in cm^{-1}) at each q-point and each branch index (ν) (calculated with uMLFF and DFT from JARVIS-DFT) and N_q represents the number of wavevectors along the q-path. In addition to automatically calculating the error metrics, our workflow will create entries for the JARVIS-Leaderboard in the appropriate format (.json.zip and .csv.zip files with the proper naming convention). From here, these entries can be directly uploaded to the leaderboard and compared to other benchmarks. Although we use JARVIS-DFT for the initial structures and calculation of the error metrics, our CHIPS-FF platform is flexible to use other datasets for initial structures and ground truth comparison. Our CHIPS-FF package offers easy-to-use command line tools, which can easily be parallelized to simultaneously run hundreds or even thousands of materials/uMLFFs on CPU and GPU.

For our benchmarking study, we chose a set of 104 materials most commonly found in semiconductor devices and interfaces. This test set contains metals, semiconductors and insulators to be representative of the various parts and interfaces of integrated circuits (semiconductor/insulator interfaces, semiconductor/metal contacts, etc.). Fig. S1 depicts various distributions of properties of the test set, including space group, band gap (calculated with

vdW-DF-optB88), atomic number, chemical formula type, crystal system, and Wyckoff site, and dimensionality, all obtained from JARVIS-DFT. In addition, Table S1 and S2 give detailed information of the chemical composition, crystal structure and band gap for each material, where we see that the set contains 28 metals (zero band gap), 14 insulators (band gap above 3 eV) and 62 semiconductors (band gap between 0 eV and 3 eV). In addition, we see from Fig. S1 that our test set represents a diverse set of materials ideal for testing our uMLFF workflow.

When considering the use of a pretrained uMLFF, the most important considerations should be accuracy, rate of convergence, scalability, and computational cost. After running the full CHIPS-FF workflow for the test set of 104 materials, we performed an analysis of which structural relaxation calculations reached convergence (force-maximum threshold of $0.05 \text{ eV}/\text{\AA}$ within 200 steps) for bulk materials, surfaces and vacancies. This analysis is presented in Table 1, where the percentage of unconverged results is depicted for each calculation type. Aside from ALIGNN-FF, all other uMLFF have a near-perfect convergence rate for bulk structures. With regards to surface and defect calculations, the convergence rate is more variable. Interestingly, the OMat24 models significantly vary in terms of convergence for surfaces and defects depending on training data. The OMat24 models trained on OMat+MPTrj+sAlexandria have a significantly higher rate of convergence when compared to the models solely trained on OMat. ORB and CHGNet have a successful rate of convergence compared to other models, which is remarkable due to the fact that the computational cost is so low (see Table 1). This is especially important since the computational cost of optimizing surfaces and defect structures greatly outweighs bulk unit cells.

For each of the 104 structures, we performed structural relaxations, fitting of the energy vs. volume curve (equation of state), calculation of the elastic tensor, calculation of the phonon band structure, relaxation of all nonpolar surfaces (among $[1, 0, 0]$, $[1, 1, 1]$, $[1, 1, 0]$, $[0, 1, 1]$, $[0, 0, 1]$, and $[0, 1, 0]$), and relaxation of each type of point defect in the material. The computational timing and errors in the lattice constants, elastic properties

and phonons for each uMLFF model are depicted in Table 2. Out of the 104 materials in our test set, there were 85 matching entries for DFT phonon calculations in JARVIS, from which the composite MAE of the phonon band structure was computed in Table 2. For most structural and phonon properties, the OMat24 models perform exceedingly well, but are the most computationally intensive. Fitting the equation of state to obtain bulk modulus and calculating the elastic tensor prove to be a more challenging task for these uMLFF models, emphasizing difficulties in modeling the potential energy landscape far from equilibrium. We found that models such as MACE-Alexandria and MatGL have superior performance in predicting the energy vs. volume curves compared to the OMat and ORB models. For contributions to the elastic tensor (C11 and C44), we also observe relatively high errors. We see that only a few models can simultaneously predict C11 and C44 with reasonable accuracy (MAE less than 50 GPa). Interestingly, we find that eqV2_31M_omat, eqV2_86M_omat and eqV2_153M_omat can predict C44 with reasonable accuracy, but have much higher prediction errors for C11, while eqV2_31M_omat_mp_salex and eqV2_86M_omat_mp_salex do a better job at predicting C11 and C44 simultaneously. We observe that MACE-MPA-0 and MatterSim give the best results for simultaneous C11 and C44 predictions.

Excellent results for structural parameters and phonons are reported for orb-v2 and MatterSim at $\approx 10 - 100$ times less the computational cost of the OMat24 models. ORB and MatterSim offer similar performance in terms of predicting phonon band structure when compared to several equivariant uMLFFs such as MACE, OMat24 and SevenNet. This is especially interesting since ORB and MatterSim-v1 are not equivariant uMLFFs. In addition, we see improved phonon results for the newer MACE-MPA-0 when compared to MACE-MP-0. Recently, it was reported that OMat and ORB models had substantial errors in phonon predictions when compared to models such as MatterSim, MACE, CHGNet, and SevenNet for 10,000 materials.⁹⁰ It is entirely possible that ORB and OMat models can predict accurate phonons for our limited test set (104 materials) but fail for a broader and more diverse set of materials.

One interesting trend we observe in our results for this set of 104 materials is that the error for lattice constant c is substantially higher than a and b . This can be due in part to the test set containing a significant portion ($\approx 10\%$) of vdW bonded (“2D-bulk-like”) layered structures (see Fig. S1). Since most of these uMLFF were trained on PBE data without vdW corrections (with the exception of ALIGNN-FF), we can expect larger errors for vdW systems. For example, we observe significant errors for hexagonal BN (JVASP-62940) when relaxed with orb-v2. This calculation did not converge within 200 steps and in the final step we observed over 130% error in c . Aside from this problematic structure (considering only the 103 structures that did converge during structural relaxation with ORB), the ORB MAE for c was 0.08 \AA . Fortunately, some of these models such as MACE and ORB have explicit dispersion corrections that can be added to more accurately address vdW interactions.^{54,55,68,69} To test this, we ran the workflow for dispersion corrected orb-d3-v2. For orb-d3-v2, all 104 bulk structures converged and we observe a significant reduction in error for c (0.048 \AA) and volume (1.90 \AA^3). For JVASP-62940 relaxed with orb-d3-v2, the percent error in c is 0.5%. This emphasizes the importance of dispersion corrections in uMLFF architectures for vdW bonded materials. An interactive version of these results is available on the JARVIS-Leaderboard platform (see Fig. 2b) for Pearson Correlation Coefficient metric), where it will be continuously updated as new uMLFF models are developed and released.

In addition to summing the computational timing for the entire workflow, we also examined the scaling behavior of each uMLFF (on CPU). These results for supercells of Cu (up to 10,000 atoms) are depicted in Fig. 2a). Unsurprisingly, we see that OMat model scales much more drastically with system size as compared to the other uMLFF models. In addition, we find that the invariant models have more favorable scaling than the equivariant models such as MACE and SevenNet, with SevenNet having slightly better scaling than MACE. The scalability of ORB and MatterSim is a huge advantage due to their accuracy of various material property predictions. Similar scalability studies were conducted in Ref.⁵⁵ The quan-

tities of surface energy and vacancy formation energy are difficult to predict with machine learning methods and provide a rigorous benchmarking test for uMLFF architectures. Out of the 104 materials, there exists 85 entries for surface DFT calculations and 48 entries for defect DFT calculations within JARVIS-DFT. We used these calculations to compare our uMLFF results. Fig. 3a) and Fig. 3b) depict the parity plots and corresponding MAE for surface energy and vacancy formation energy of our test sets. The very low error for surface energy (0.18 J/m²) and vacancy formation energy (0.94 eV) highlight some of the successes of recent state-of-the-art models such as OMat24, ORB, MACE-MPA-0 and MatterSim. We also observe generally good results for MACE-MP-0 and SevenNet when predicting vacancy formation energy and surface energies. The low cost of ORB, high rate of convergence and high accuracy make it a viable tool to relax larger surfaces and defect supercells.

In addition to benchmarking the properties of bulk materials, we utilized the CHIPS-FF workflow for interface calculations. Fig. 3c depicts the parity plot for work of adhesion (W_{ad}) for various material interfaces. The MAE for W_{ad} is computed with respect to “ground truth” data taken from Ref.¹¹³ (from experiment and theory). As seen in Fig. 3c, predictions for W_{ad} are extremely poor for each uMLFF type. This is not surprising due to the fact that none of these uMLFF are trained on interface data. We went on to analyze one of the best performing predictions for an Al(111)Al₂O₃(001) interface (see red box on Fig. 3c). From here, we performed an in-plane (xy) grid search to find the optimal energy configuration of the interface. In addition, this in-plane scan can be a test of how smooth the potential energy surface is. On the right panel of Fig. 3c we see the results of this interface scan for a number of uMLFFs. We observe a smoother potential energy surface for MACE, SevenNet, MatterSim and OMat24 models. Although the MAE is extremely high for all uMLFF models for W_{ad} , it is the lowest for ALIGNN-FF. This can be due in part to ALIGNN-FF being trained on vdW-corrected DFT calculations and having a substantial amount of exfoliable materials in the dataset.

We chose to benchmark the performance of uMLFF models for the generation of amor-

phous Si (a-Si) by performing melt/quench simulations. Fig. 4 depicts a summary of these results, where the radial distribution function (RDF) is shown as a function of pair separation distance. We benchmarked these uMLFF RDF curves against the RDF curve obtained from computationally expensive AIMD simulations for a-Si. The inset of Fig. 4 depicts the MAE of each RDF curve with respect to AIMD. We observe that architectures such as MACE, SevenNet, and OMat24 (eqV2), CHGNet, ALIGNN-FF, MatterSim and ORB have excellent accuracy, while MatGL has a slightly higher MAE and a lower R^2 value. The final amorphous structures for AIMD, MatterSim, eqV2 and ORB (best performing uMLFF models) are given in the inset of Fig. 4. The exceptional performance of ORB and MatterSim (both invariant uMLFFs) for a-Si is significant due to the fact that it is much less costly than other similarly performing equivariant uMLFF models. The relatively high accuracy of ALIGNN-FF with regards to a-Si is surprising due to the fact that ALIGNN-FF had inferior performance for a number of properties and is also an invariant model. A more thorough assessment of how ALIGNN-FF and other uMLFFs can model amorphous materials will be the subject of future work, which will also utilize the CHIPS-FF infrastructure. These results bring into question whether or not equivariance is necessary to achieve accurate results for amorphous materials with uMLFFs, and more rigorous benchmarking will need to be conducted to bring clarity to this.

In addition to testing these uMLFF models on a smaller and more focused dataset, we also tested on a larger and more diverse dataset for force predictions. Unlike total energy, forces are more independent of exchange-correlation functional and the accuracy of force predictions on various datasets can give valuable insight into how a particular model performs. We chose to benchmark each uMLFF on the MLEARN dataset from Ref.,¹¹⁴ which consists of face-centered cubic (Cu, Ni) and body-centered cubic (Li, Mo) metals and diamond group IV semiconductors (Si, Ge) which span a wide range of crystal structures and bonding environments ($\approx 200 - 300$ data points for each element). These results are depicted in Table 3. In addition, we benchmarked the accuracy of force predictions on very

large datasets that were used to train uMLFFs. These datasets included ALIGNN_FF_DB (307,000 used to train ALIGNN-FF), MPF (188,000 used to train M3GNet), and MPTrj (1.58 million used to train CHGNet, MACE, SevenNet and used in the training of ORB and OMat models). These results are depicted in Table 4. Unsurprisingly, superior accuracy is obtained across all datasets when the OMat and ORB models are used to predict forces. We also observe highly accurate forces for MatterSim and a substantial reduction in force error when going from MACE-MP-0 to MACE-MPA-0. The CHIPS-FF package has built in functions to perform these benchmarking calculations on each respective dataset, with a flexible framework to add additional datasets (such as OMat and Alexandria) and new uMLFFs as they develop over time.

Table 3: A comparison of force errors (eV/Å) and timings (s) for the mlearn DFT dataset for Mo, Li, Si, Ni, Cu, and Ge. The green color highlights the best performing model for each element.

uMLFF Type	Mo		Li		Si		Ni		Cu		Ge	
	Error (eV/Å)	Time (s)	Error (eV/Å)	Time (s)	Error (eV/Å)	Time (s)	Error (eV/Å)	Time (s)	Error (eV/Å)	Time (s)	Error (eV/Å)	Time (s)
alignn_ff	0.869	1.2×10^2	0.122	9.5×10^1	0.324	9.5×10^1	0.303	2.1×10^2	0.216	1.9×10^2	0.395	4.5×10^1
chgnet	0.361	9.9×10^1	0.045	1.4×10^2	0.188	3.6×10^1	0.059	3.1×10^2	0.058	2.9×10^2	0.207	3.3×10^1
eqV2_153M_omat	0.096	3.0×10^3	0.004	3.5×10^3	0.012	6.6×10^3	0.009	1.8×10^4	0.006	9.2×10^3	0.031	4.6×10^3
eqV2_31M_omat	0.098	6.9×10^2	0.004	7.9×10^2	0.016	3.2×10^3	0.010	3.4×10^3	0.005	2.1×10^3	0.033	1.1×10^3
eqV2_31M_omat_mp_salex	0.056	6.9×10^2	0.007	7.9×10^2	0.021	2.2×10^3	0.011	2.1×10^3	0.006	3.9×10^3	0.028	1.1×10^3
eqV2_86M_omat	0.094	1.8×10^3	0.004	2.0×10^3	0.014	9.3×10^3	0.009	9.9×10^2	0.006	5.5×10^3	0.032	2.7×10^3
eqV2_86M_omat_mp_salex	0.048	1.8×10^3	0.005	2.0×10^3	0.016	4.9×10^3	0.009	5.5×10^3	0.005	9.7×10^3	0.030	2.7×10^3
mace	0.292	2.6×10^2	0.035	2.8×10^2	0.149	1.9×10^2	0.055	1.8×10^3	0.059	5.5×10^2	0.203	1.9×10^2
mace-alexandria	0.343	4.3×10^2	0.025	4.7×10^2	0.202	1.1×10^3	0.099	2.2×10^3	0.055	2.1×10^3	0.161	9.4×10^2
mace-mpa	0.130	2.1×10^2	0.014	2.5×10^2	0.083	3.5×10^2	0.026	7.6×10^2	0.013	7.4×10^2	0.063	3.5×10^2
matgl	0.333	1.0×10^1	0.042	2.1×10^1	0.226	4.1×10^1	0.069	7.4×10^1	0.124	6.5×10^1	0.299	2.2×10^1
matgl-direct	0.300	3.8×10^1	0.031	3.9×10^1	0.214	4.7×10^1	0.114	1.6×10^2	0.054	1.4×10^2	0.260	4.8×10^1
mattersim	0.121	1.2×10^2	0.024	2.2×10^1	0.067	1.5×10^2	0.021	5.3×10^2	0.012	4.6×10^2	0.068	1.3×10^2
orb-v2	0.130	1.1×10^2	0.018	1.2×10^2	0.068	1.4×10^2	0.026	2.8×10^2	0.015	2.8×10^2	0.060	1.4×10^2
sevennet	0.365	1.9×10^2	0.051	1.4×10^2	0.129	1.4×10^2	0.089	8.4×10^2	0.055	3.7×10^2	0.131	1.4×10^2

We have introduced CHIPS-FF, an open-source benchmarking platform for MLFF architectures, which has the capability to test properties beyond the standard total energy, including forces, phonons, elastic properties, surface energy, vacancy formation energy and properties of interfaces. We benchmarked several recent state-of-the-art uMLFF architectures on a subset of 104 materials most relevant for the semiconductor industry, taking into account accuracy with respect to DFT, convergence and computational cost. As MLFFs continue to develop over time, we expect the CHIPS-FF benchmarking platform to be critical

Table 4: A comparison of force errors (eV/Å) and timings (s) for different datasets: ALIGNN_FF_DB, MPF, and MPTrj. The green color highlights the best performing model.

MLFF Type	ALIGNN_FF_DB (307k)		MPF (188k)		MPTrj (1.58M)	
	Error (eV/Å)	Time (s)	Error (eV/Å)	Time (s)	Error (eV/Å)	Time (s)
alignn_ff	0.472	2.9×10^4	0.639	4.1×10^4	0.581	3.5×10^5
chgnet	0.088	3.2×10^4	0.101	1.1×10^5	0.060	7.6×10^5
eqV2_153M_omat	0.050	1.5×10^6	-	-	-	-
eqV2_31M_omat	0.051	3.0×10^5	0.046	3.5×10^5	-	-
eqV2_31M_omat_mp_salex	0.055	3.9×10^5	0.032	4.3×10^5	-	-
eqV2_86M_omat	0.052	9.2×10^5	0.043	9.3×10^5	-	-
eqV2_86M_omat_mp_salex	0.056	9.2×10^5	-	-	-	-
mace	0.104	5.0×10^4	0.125	1.8×10^5	0.059	1.1×10^6
mace-alexandria	0.221	1.3×10^5	0.395	2.7×10^5	-	-
mace-mpa	0.072	7.0×10^5	0.061	1.3×10^5	-	-
matgl	0.091	1.1×10^4	0.066	3.4×10^4	0.100	1.4×10^5
matgl-direct	0.104	1.7×10^4	0.095	4.2×10^4	0.118	2.7×10^5
mattersim	0.071	8.7×10^4	0.047	7.1×10^4	0.059	1.7×10^6
orb-v2	0.062	5.0×10^4	0.049	8.4×10^4	0.028	7.5×10^5
sevnet	0.092	4.4×10^4	0.081	6.0×10^4	0.041	5.0×10^5

in terms of testing the quality of uMLFFs.

Data Availability Statement

The CHIPS-FF package can be found at <https://github.com/usnistgov/chipsff>. All data specific to this work will be made available on Figshare upon publication. Related benchmarks for this work can be found at https://pages.nist.gov/jarvis_leaderboard/Special/CHIPS_FF/.

Conflicts of Interest

The authors declare no competing interests.

Acknowledgments

All authors thank the National Institute of Standards and Technology for funding, computational, and data-management resources. This work was performed with funding from the CHIPS Metrology Program, part of CHIPS for America, National Institute of Standards and Technology, U.S. Department of Commerce. Certain commercial equipment, instruments, software, or materials are identified in this paper in order to specify the experimental procedure adequately. Such identifications are not intended to imply recommendation or endorsement by NIST, nor it is intended to imply that the materials or equipment identified are necessarily the best available for the purpose. The authors would like to acknowledge John Bonini for a fruitful discussion regarding the manuscript and software package.

References

- (1) Tadmor, E. B.; Miller, R. E. *Modeling materials: continuum, atomistic and multiscale techniques*; Cambridge University Press, 2011.
- (2) Xia, W.; Pestana, L. A. R. *Fundamentals of Multiscale Modeling of Structural Materials*; Elsevier, 2022.
- (3) National Institute of Standards and Technology (NIST), NIST CHIPS Program. <https://www.nist.gov/chips>, 2024; Accessed: 2024-10-02.
- (4) Martin, R. M. *Electronic structure: basic theory and practical methods*; Cambridge university press, 2020.
- (5) Allen, M. P.; Tildesley, D. J. *Computer simulation of liquids*; Oxford university press, 2017.
- (6) Vasileska, D.; Goodnick, S. M.; Klimeck, G. *Computational Electronics: semiclassical and quantum device modeling and simulation*; CRC press, 2017.

- (7) Butler, K. T.; Oviedo, F.; Canepa, P. *Machine Learning in Materials Science*; ACS In Focus; American Chemical Society, 2021; pp –1.
- (8) Jacobs, R.; Schultz, L. E.; Scourtas, A.; Schmidt, K.; Price-Skelly, O.; Engler, W.; Foster, I.; Blaiszik, B.; Voyles, P. M.; Morgan, D. Machine learning materials properties with accurate predictions, uncertainty estimates, domain guidance, and persistent online accessibility. *Machine Learning: Science and Technology* **2024**, *5*, 045051.
- (9) Schmidt, J.; Marques, M. R. G.; Botti, S.; Marques, M. A. L. Recent advances and applications of machine learning in solid-state materials science. *npj Computational Materials* **2019**, *5*, 83.
- (10) Choudhary, K.; DeCost, B.; Chen, C.; Jain, A.; Tavazza, F.; Cohn, R.; Park, C. W.; Choudhary, A.; Agrawal, A.; Billinge, S. J., et al. Recent advances and applications of deep learning methods in materials science. *npj Computational Materials* **2022**, *8*, 59.
- (11) Han, X.-Q.; Wang, X.-D.; Xu, M.-Y.; Feng, Z.; Yao, B.-W.; Guo, P.-J.; Gao, Z.-F.; Lu, Z.-Y. AI-driven inverse design of materials: Past, present and future. 2024; <https://arxiv.org/abs/2411.09429>.
- (12) Choudhary, K. Atomgpt: Atomistic generative pretrained transformer for forward and inverse materials design. *The Journal of Physical Chemistry Letters* **2024**, *15*, 6909–6917.
- (13) Jablonka, K. M. et al. 14 examples of how LLMs can transform materials science and chemistry: a reflection on a large language model hackathon. *Digital Discovery* **2023**, *2*, 1233–1250.
- (14) Lyons, J. L.; Van de Walle, C. G. Computationally predicted energies and properties of defects in GaN. *npj Computational Materials* **2017**, *3*, 12.

- (15) Buckeridge, J. Equilibrium point defect and charge carrier concentrations in a material determined through calculation of the self-consistent Fermi energy. *Computer Physics Communications* **2019**, *244*, 329–342.
- (16) Choudhary, K.; Sumpter, B. G. Can a deep-learning model make fast predictions of vacancy formation in diverse materials? *AIP Advances* **2023**, *13*, 095109.
- (17) Rahman, M. H.; Gollapalli, P.; Manganaris, P.; Yadav, S. K.; Pilania, G.; DeCost, B.; Choudhary, K.; Mannodi-Kanakkithodi, A. Accelerating defect predictions in semiconductors using graph neural networks. *APL Machine Learning* **2024**, *2*, 016122.
- (18) Turiansky, M. E.; Alkauskas, A.; Engel, M.; Kresse, G.; Wickramaratne, D.; Shen, J.-X.; Dreyer, C. E.; Van de Walle, C. G. Nonrad: Computing nonradiative capture coefficients from first principles. *Computer Physics Communications* **2021**, *267*, 108056.
- (19) Broberg, D.; Bystrom, K.; Srivastava, S.; Dahliah, D.; Williamson, B. A. D.; Weston, L.; Scanlon, D. O.; Rignanese, G.-M.; Dwaraknath, S.; Varley, J.; Persson, K. A.; Asta, M.; Hautier, G. High-throughput calculations of charged point defect properties with semi-local density functional theory—performance benchmarks for materials screening applications. *npj Computational Materials* **2023**, *9*, 72.
- (20) Liu, Z.-F. Density functional descriptions of interfacial electronic structure. *Chemical Physics Reviews* **2023**, *4*, 031307.
- (21) Choudhary, K.; Garrity, K. F. InterMat: accelerating band offset prediction in semiconductor interfaces with DFT and deep learning. *Digital Discovery* **2024**, *3*, 1365–1377.
- (22) Park, J.-S.; Jung, Y.-K.; Butler, K. T.; Walsh, A. Quick-start guide for first-principles modelling of semiconductor interfaces. *Journal of Physics: Energy* **2018**, *1*, 016001.

- (23) Butler, K. T.; Sai Gautam, G.; Canepa, P. Designing interfaces in energy materials applications with first-principles calculations. *npj Computational Materials* **2019**, *5*, 19.
- (24) Hinuma, Y.; Grüneis, A.; Kresse, G.; Oba, F. Band alignment of semiconductors from density-functional theory and many-body perturbation theory. *Phys. Rev. B* **2014**, *90*, 155405.
- (25) Tran, R.; Xu, Z.; Radhakrishnan, B.; Winston, D.; Sun, W.; Persson, K. A.; Ong, S. P. Surface energies of elemental crystals. *Scientific Data* **2016**, *3*, 160080.
- (26) Huang, J.; Lin, F.; Hin, C. Density-functional-theory approach to determine band offsets and dielectric breakdown properties across metal/crystal oxide and metal/amorphous oxide interfaces: A case study of Al/SiO₂. *Applied Surface Science* **2019**, *483*, 616–625.
- (27) Siron, M.; Chandrasekhar, N.; Persson, K. A. Enabling automated high-throughput Density Functional Theory studies of amorphous material surface reactions. *Computational Materials Science* **2023**, *226*, 112192.
- (28) Deringer, V. L.; Bernstein, N.; Bartók, A. P.; Cliffe, M. J.; Kerber, R. N.; Marbella, L. E.; Grey, C. P.; Elliott, S. R.; Csányi, G. Realistic Atomistic Structure of Amorphous Silicon from Machine-Learning-Driven Molecular Dynamics. *The Journal of Physical Chemistry Letters* **2018**, *9*, 2879–2885.
- (29) Zheng, H.; Sivonxay, E.; Gallant, M.; Luo, Z.; McDermott, M.; Huck, P.; Persson, K. A. The ab initio amorphous materials database: Empowering machine learning to decode diffusivity. 2024; <https://arxiv.org/abs/2402.00177>.
- (30) Hong, S. et al. Ultralow-dielectric-constant amorphous boron nitride. *Nature* **2020**, *582*, 511–514.

- (31) Khot, A. C.; Dongale, T. D.; Nirmal, K. A.; Sung, J. H.; Lee, H. J.; Nikam, R. D.; Kim, T. G. Amorphous Boron Nitride Memristive Device for High-Density Memory and Neuromorphic Computing Applications. *ACS Applied Materials & Interfaces* **2022**, *14*, 10546–10557.
- (32) Rappe, A. K.; Casewit, C. J.; Colwell, K. S.; Goddard, W. A. I.; Skiff, W. M. UFF, a full periodic table force field for molecular mechanics and molecular dynamics simulations. *Journal of the American Chemical Society* **1992**, *114*, 10024–10035.
- (33) Behler, J.; Parrinello, M. Generalized neural-network representation of high-dimensional potential-energy surfaces. *Physical review letters* **2007**, *98*, 146401.
- (34) Bartók, A. P.; Payne, M. C.; Kondor, R.; Csányi, G. Gaussian approximation potentials: The accuracy of quantum mechanics, without the electrons. *Physical review letters* **2010**, *104*, 136403.
- (35) Wood, M. A.; Thompson, A. P. Extending the accuracy of the SNAP interatomic potential form. *The Journal of chemical physics* **2018**, *148*, 241721.
- (36) Musaelian, A.; Batzner, S.; Johansson, A.; Sun, L.; Owen, C. J.; Kornbluth, M.; Kozinsky, B. Learning local equivariant representations for large-scale atomistic dynamics. *Nature Communications* **2023**, *14*, 579.
- (37) Jain, A.; Ong, S. P.; Hautier, G.; Chen, W.; Richards, W. D.; Dacek, S.; Cholia, S.; Gunter, D.; Skinner, D.; Ceder, G.; Persson, K. A. Commentary: The Materials Project: A materials genome approach to accelerating materials innovation. *APL Materials* **2013**, *1*, 011002.
- (38) Wines, D.; Gurunathan, R.; Garrity, K. F.; DeCost, B.; Biacchi, A. J.; Tavazza, F.; Choudhary, K. Recent progress in the JARVIS infrastructure for next-generation data-driven materials design. *Applied Physics Reviews* **2023**, *10*, 041302.

- (39) Choudhary, K. et al. The joint automated repository for various integrated simulations (JARVIS) for data-driven materials design. *npj Computational Materials* **2020**, *6*, 173.
- (40) Saal, J. E.; Kirklin, S.; Aykol, M.; Meredig, B.; Wolverton, C. Materials Design and Discovery with High-Throughput Density Functional Theory: The Open Quantum Materials Database (OQMD). *JOM* **2013**, *65*, 1501–1509.
- (41) Kirklin, S.; Saal, J. E.; Meredig, B.; Thompson, A.; Doak, J. W.; Aykol, M.; Rühl, S.; Wolverton, C. The Open Quantum Materials Database (OQMD): assessing the accuracy of DFT formation energies. *npj Computational Materials* **2015**, *1*, 15010.
- (42) Schmidt, J.; Hoffmann, N.; Wang, H.-C.; Borlido, P.; Carriço, P. J. M. A.; Cerqueira, T. F. T.; Botti, S.; Marques, M. A. L. Machine-Learning-Assisted Determination of the Global Zero-Temperature Phase Diagram of Materials. *Advanced Materials* **2023**, *35*, 2210788.
- (43) Wang, H.-C.; Schmidt, J.; Marques, M. A. L.; Wirtz, L.; Romero, A. H. Symmetry-based computational search for novel binary and ternary 2D materials. *2D Materials* **2023**, *10*, 035007.
- (44) Schmidt, J.; Pettersson, L.; Verdozzi, C.; Botti, S.; Marques, M. A. L. Crystal graph attention networks for the prediction of stable materials. *Science Advances* **2021**, *7*, eabi7948.
- (45) Schmidt, J.; Cerqueira, T. F.; Romero, A. H.; Loew, A.; Jäger, F.; Wang, H.-C.; Botti, S.; Marques, M. A. Improving machine-learning models in materials science through large datasets. *Materials Today Physics* **2024**, *48*, 101560.
- (46) Deng, B.; Choi, Y.; Zhong, P.; Riebesell, J.; Anand, S.; Li, Z.; Jun, K.; Persson, K. A.; Ceder, G. Systematic softening in universal machine learning interatomic potentials. *npj Computational Materials* **2025**, *11*, 9.

- (47) Focassio, B.; M. Freitas, L. P.; Schleder, G. R. Performance Assessment of Universal Machine Learning Interatomic Potentials: Challenges and Directions for Materials' Surfaces. *ACS Applied Materials & Interfaces* **2024**,
- (48) Casillas-Trujillo, L.; Parackal, A. S.; Armiento, R.; Alling, B. Evaluating and improving the predictive accuracy of mixing enthalpies and volumes in disordered alloys from universal pretrained machine learning potentials. *Phys. Rev. Mater.* **2024**, *8*, 113803.
- (49) Wines, D.; Choudhary, K. Data-driven design of high pressure hydride superconductors using DFT and deep learning. *Materials futures* **2024**, *3*, 025602.
- (50) Wang, S.-H.; Xin, H.; Achenie, L.; Choudhary, K. Examining Generalizability of AI Models for Catalysis. **2024**,
- (51) Pota, B.; Ahlawat, P.; Csanyi, G.; Simoncelli, M. Thermal Conductivity Predictions with Foundation Atomistic Models. 2024; <https://arxiv.org/abs/2408.00755>.
- (52) Gruver, N.; Sriram, A.; Madotto, A.; Wilson, A. G.; Zitnick, C. L.; Ulissi, Z. Fine-tuned language models generate stable inorganic materials as text. *arXiv preprint arXiv:2402.04379* **2024**,
- (53) Elrashidy, A.; Della-Giustina, J.; Yan, J.-A. Accelerated Data-Driven Discovery and Screening of Two-Dimensional Magnets Using Graph Neural Networks. *The Journal of Physical Chemistry C* **2024**, *128*, 6007–6018.
- (54) Batatia, I. et al. A foundation model for atomistic materials chemistry. 2024; <https://arxiv.org/abs/2401.00096>.
- (55) Neumann, M.; Gin, J.; Rhodes, B.; Bennett, S.; Li, Z.; Choubisa, H.; Hussey, A.; Godwin, J. Orb: A Fast, Scalable Neural Network Potential. 2024; <https://arxiv.org/abs/2410.22570>.

- (56) Team, F.-C. OMat24 Model. <https://huggingface.co/fairchem/OMAT24>, 2024; <https://huggingface.co/fairchem/OMAT24>, Accessed: 2024-10-22.
- (57) Chen, C.; Zuo, Y.; Ye, W.; Li, X.; Ong, S. P. Learning properties of ordered and disordered materials from multi-fidelity data. *Nature Computational Science* **2021**, *1*, 46–53.
- (58) Choudhary, K.; DeCost, B. Atomistic Line Graph Neural Network for improved materials property predictions. *npj Computational Materials* **2021**, *7*, 185.
- (59) Garrity, K. F.; Choudhary, K. Fast and accurate prediction of material properties with three-body tight-binding model for the periodic table. *Phys. Rev. Mater.* **2023**, *7*, 044603.
- (60) Seifert, G. Tight-Binding Density Functional Theory: An Approximate Kohn-Sham DFT Scheme. *The Journal of Physical Chemistry A* **2007**, *111*, 5609–5613.
- (61) Chen, C.; Ong, S. P. A universal graph deep learning interatomic potential for the periodic table. *Nature Computational Science* **2022**, *2*, 718–728.
- (62) Materials Virtual Lab, MatGL: Graph Learning for Materials Science. <https://github.com/materialsvirtuallab/matgl>, 2024; Accessed: 2024-10-02.
- (63) Wang, M.; Zheng, D.; Ye, Z.; Gan, Q.; Li, M.; Song, X.; Zhou, J.; Ma, C.; Yu, L.; Gai, Y.; Xiao, T.; He, T.; Karypis, G.; Li, J.; Zhang, Z. Deep Graph Library: A Graph-Centric, Highly-Performant Package for Graph Neural Networks. 2020; <https://arxiv.org/abs/1909.01315>.
- (64) Paszke, A. et al. PyTorch: An Imperative Style, High-Performance Deep Learning Library. 2019; <https://arxiv.org/abs/1912.01703>.

- (65) Chen, C.; Ye, W.; Zuo, Y.; Zheng, C.; Ong, S. P. Graph Networks as a Universal Machine Learning Framework for Molecules and Crystals. *Chemistry of Materials* **2019**, *31*, 3564–3572.
- (66) Choudhary, K.; DeCost, B.; Major, L.; Butler, K.; Thiyagalingam, J.; Tavazza, F. Unified graph neural network force-field for the periodic table: solid state applications. *Digital Discovery* **2023**, *2*, 346–355.
- (67) Deng, B.; Zhong, P.; Jun, K.; Riebesell, J.; Han, K.; Bartel, C. J.; Ceder, G. CHGNet as a pretrained universal neural network potential for charge-informed atomistic modelling. *Nature Machine Intelligence* **2023**, *5*, 1031–1041.
- (68) Batatia, I.; Kovacs, D. P.; Simm, G. N. C.; Ortner, C.; Csanyi, G. MACE: Higher Order Equivariant Message Passing Neural Networks for Fast and Accurate Force Fields. *Advances in Neural Information Processing Systems*. 2022.
- (69) Batatia, I.; Batzner, S.; Kovács, D. P.; Musaelian, A.; Simm, G. N. C.; Drautz, R.; Ortner, C.; Kozinsky, B.; Csányi, G. The Design Space of E(3)-Equivariant Atom-Centered Interatomic Potentials. 2022.
- (70) Drautz, R. Atomic cluster expansion for accurate and transferable interatomic potentials. *Phys. Rev. B* **2019**, *99*, 014104.
- (71) Dusson, G.; Bachmayr, M.; Csányi, G.; Drautz, R.; Etter, S.; van der Oord, C.; Ortner, C. Atomic cluster expansion: Completeness, efficiency and stability. *Journal of Computational Physics* **2022**, *454*, 110946.
- (72) Team, A. MACE-MP: ACE Multi-Physics Framework. https://github.com/ACESuit/mace-mp/releases/tag/mace_mpa_0, 2024; https://github.com/ACESuit/mace-mp/releases/tag/mace_mpa_0, Version 0 release.

- (73) Park, Y.; Kim, J.; Hwang, S.; Han, S. Scalable Parallel Algorithm for Graph Neural Network Interatomic Potentials in Molecular Dynamics Simulations. *Journal of Chemical Theory and Computation* **2024**, *20*, 4857–4868.
- (74) Batzner, S.; Musaelian, A.; Sun, L.; Geiger, M.; Mailoa, J. P.; Kornbluth, M.; Molinari, N.; Smidt, T. E.; Kozinsky, B. E(3)-equivariant graph neural networks for data-efficient and accurate interatomic potentials. *Nature Communications* **2022**, *13*, 2453.
- (75) Yang, H. et al. MatterSim: A Deep Learning Atomistic Model Across Elements, Temperatures and Pressures. 2024; <https://arxiv.org/abs/2405.04967>.
- (76) Merchant, A.; Batzner, S.; Schoenholz, S. S.; Aykol, M.; Cheon, G.; Cubuk, E. D. Scaling deep learning for materials discovery. *Nature* **2023**, *624*, 80–85.
- (77) Microsoft, MatterSim: Simulator for Visual Language Navigation. <https://github.com/microsoft/mattersim>, 2024; Accessed: 2024-12-06.
- (78) Orbital Materials, Orb-Models: Machine Learning Models for Orbital Materials. <https://github.com/orbital-materials/orb-models>, 2024; Accessed: 2024-10-02.
- (79) Orbital Materials, Introducing the Orb AI-Based Interatomic Potential. <https://www.orbitalmaterials.com/post/technical-blog-introducing-the-orb-ai-based-interatomic-potential>, 2024; Accessed: 2024-10-02.
- (80) Riebesell, J.; Goodall, R.; Benner, P.; Chiang, Y.; Deng, B.; Lee, A.; Jain, A.; Persson, K. Matbench Discovery: A Benchmark for AI-Accelerated Materials Discovery. <https://matbench-discovery.materialsproject.org/preprint>, 2024; Accessed: 2024-10-02.

- (81) Sanchez-Gonzalez, A.; Godwin, J.; Pfaff, T.; Ying, R.; Leskovec, J.; Battaglia, P. W. Learning to Simulate Complex Physics with Graph Networks. 2020; <https://arxiv.org/abs/2002.09405>.
- (82) Gilmer, J.; Schoenholz, S. S.; Riley, P. F.; Vinyals, O.; Dahl, G. E. Neural Message Passing for Quantum Chemistry. 2017; <https://arxiv.org/abs/1704.01212>.
- (83) Barroso-Luque, L.; Shuaibi, M.; Fu, X.; Wood, B. M.; Dzamba, M.; Gao, M.; Rizvi, A.; Zitnick, C. L.; Ulissi, Z. W. Open Materials 2024 (OMat24) Inorganic Materials Dataset and Models. 2024; <https://arxiv.org/abs/2410.12771>.
- (84) Liao, Y.-L.; Wood, B.; Das, A.; Smidt, T. EquiformerV2: Improved Equivariant Transformer for Scaling to Higher-Degree Representations. 2024; <https://arxiv.org/abs/2306.12059>.
- (85) Riebesell, J.; Goodall, R. E. A.; Benner, P.; Chiang, Y.; Deng, B.; Lee, A. A.; Jain, A.; Persson, K. A. Matbench Discovery – A framework to evaluate machine learning crystal stability predictions. 2024; <https://arxiv.org/abs/2308.14920>.
- (86) Choudhary, K. et al. JARVIS-Leaderboard: a large scale benchmark of materials design methods. *npj Computational Materials* **2024**, *10*, 93.
- (87) National Institute of Standards and Technology (NIST), JARVIS Leaderboard: Benchmarking Models for Materials Science. https://pages.nist.gov/jarvis_leaderboard/, 2024; Accessed: 2024-10-02.
- (88) Yu, H.; Giantomassi, M.; Materzanini, G.; Wang, J.; Rignanese, G.-M. Systematic assessment of various universal machine-learning interatomic potentials. *Materials Genome Engineering Advances* *n/a*, e58.
- (89) Zhu, S.; Arróyave, R.; Saritürk, D. Accelerating CALPHAD-based Phase Diagram

- Predictions in Complex Alloys Using Universal Machine Learning Potentials: Opportunities and Challenges. 2024; <https://arxiv.org/abs/2411.15351>.
- (90) Loew, A.; Sun, D.; Wang, H.-C.; Botti, S.; Marques, M. A. L. Universal Machine Learning Interatomic Potentials are Ready for Phonons. 2024; <https://arxiv.org/abs/2412.16551>.
- (91) Choudhary, K.; Kalish, I.; Beams, R.; Tavazza, F. High-throughput Identification and Characterization of Two-dimensional Materials using Density functional theory. *Scientific Reports* **2017**, *7*, 5179.
- (92) Perdew, J. P.; Schmidt, K. Jacob’s ladder of density functional approximations for the exchange-correlation energy. *AIP Conference Proceedings* **2001**, *577*, 1–20.
- (93) Hjorth Larsen, A. et al. The atomic simulation environment—a Python library for working with atoms. *Journal of Physics: Condensed Matter* **2017**, *29*, 273002.
- (94) Qi, J.; Ko, T. W.; Wood, B. C.; Pham, T. A.; Ong, S. P. Robust training of machine learning interatomic potentials with dimensionality reduction and stratified sampling. *npj Computational Materials* **2024**, *10*, 43.
- (95) Grimme, S.; Antony, J.; Ehrlich, S.; Krieg, H. A consistent and accurate ab initio parametrization of density functional dispersion correction (DFT-D) for the 94 elements H-Pu. *The Journal of Chemical Physics* **2010**, *132*, 154104.
- (96) Perdew, J. P.; Ruzsinszky, A.; Csonka, G. I.; Vydrov, O. A.; Scuseria, G. E.; Constantin, L. A.; Zhou, X.; Burke, K. Restoring the Density-Gradient Expansion for Exchange in Solids and Surfaces. *Phys. Rev. Lett.* **2008**, *100*, 136406.
- (97) Team, H. 2D Universal Force Field CPU Model (Alexandria v2). https://github.com/hyllios/utills/blob/main/models/alexandria_v2/mace/2D_universal_force_field_cpu.model, 2024; <https://github.com/hyllios/utills/>

blob/main/models/alexandria_v2/mace/2D_universal_force_field_cpu.model,
Model file available at GitHub.

- (98) Bitzek, E.; Koskinen, P.; Gähler, F.; Moseler, M.; Gumbsch, P. Structural Relaxation Made Simple. *Phys. Rev. Lett.* **2006**, *97*, 170201.
- (99) Jochym, P. T. Module for calculating elastic tensor of crystals. <https://github.com/jochym/Elastic/>, 2022.
- (100) Jochym, P. T.; Parlinski, K.; Sternik, M. TiC lattice dynamics from ab initio calculations. *The European Physical Journal B - Condensed Matter and Complex Systems* **1999**, *10*, 9–13.
- (101) Jochym, P. T.; Parlinski, K. Ab initio lattice dynamics and elastic constants of ZrC. *The European Physical Journal B - Condensed Matter and Complex Systems* **2000**, *15*, 265–268.
- (102) Togo, A.; Chaput, L.; Tanaka, I. Distributions of phonon lifetimes in Brillouin zones. *Phys. Rev. B* **2015**, *91*, 094306.
- (103) Togo, A.; Chaput, L.; Tadano, T.; Tanaka, I. Implementation strategies in phonopy and phono3py. *J. Phys. Condens. Matter* **2023**, *35*, 353001.
- (104) Chaput, L.; Togo, A.; Tanaka, I.; Hug, G. Phonon-phonon interactions in transition metals. *Phys. Rev. B* **2011**, *84*, 094302.
- (105) Togo, A.; Chaput, L.; Tanaka, I.; Hug, G. First-principles phonon calculations of thermal expansion in Ti_3SiC_2 , Ti_3AlC_2 , and Ti_3GeC_2 . *Phys. Rev. B* **2010**, *81*, 174301.
- (106) Kresse, G.; Furthmüller, J. Efficient Iterative Schemes for ab initio Total-energy Calculations Using a Plane-wave Basis Set. *Phys. Rev. B* **1996**, *54*, 11169–11186.
- (107) Kresse, G.; Joubert, D. From Ultrasoft Pseudopotentials to the Projector Augmented-wave Method. *Phys. Rev. B* **1999**, *59*, 1758–1775.

- (108) Van de Walle, C. G.; Martin, R. M. Theoretical study of band offsets at semiconductor interfaces. *Phys. Rev. B* **1987**, *35*, 8154–8165.
- (109) Di Liberto, G.; Pacchioni, G. Band offset in semiconductor heterojunctions. *Journal of Physics: Condensed Matter* **2021**, *33*, 415002.
- (110) Zur, A.; McGill, T. C. Lattice match: An application to heteroepitaxy. *Journal of Applied Physics* **1984**, *55*, 378–386.
- (111) Klimeš, J.; Bowler, D. R.; Michaelides, A. Chemical accuracy for the van der Waals density functional. *Journal of Physics: Condensed Matter* **2009**, *22*, 022201.
- (112) Perdew, J. P.; Burke, K.; Ernzerhof, M. Generalized Gradient Approximation Made Simple. *Phys. Rev. Lett.* **1996**, *77*, 3865–3868.
- (113) Project, U. N. I. Interface.csv dataset. <https://github.com/usnistgov/intermat/blob/temp/intermat/Interface.csv>, 2024; Accessed: 2024-10-23.
- (114) Zuo, Y.; Chen, C.; Li, X.; Deng, Z.; Chen, Y.; Behler, J.; Csányi, G.; Shapeev, A. V.; Thompson, A. P.; Wood, M. A.; Ong, S. P. Performance and Cost Assessment of Machine Learning Interatomic Potentials. *The Journal of Physical Chemistry A* **2020**, *124*, 731–745.

Supporting Information: CHIPS-FF: Evaluating Universal Machine Learning Force Fields for Material Properties

Daniel Wines* and Kamal Choudhary

*Material Measurement Laboratory, National Institute of Standards and Technology,
Gaithersburg, MD 20899, USA*

E-mail: daniel.wines@nist.gov

Table S1: A detailed description of the materials in the test set (part one), including JARVIS-ID, space group number and symbol and band gap (vdW-DF-optB88).

JID	Formula	SPG Number	SPG Symbol	optb88vdw Band Gap (eV)
JVASP-1002	Si	227	<i>Fd-3m</i>	0.731
JVASP-10036	TiO ₂	136	<i>P4₂/mmm</i>	1.769
JVASP-10037	SnO ₂	136	<i>P4₂/mnm</i>	0.894
JVASP-1008	Sn	227	<i>Fd-3m</i>	0
JVASP-1023	Te	152	<i>P3₁₂₁</i>	0.165
JVASP-1029	Ti	191	<i>P6/mmm</i>	0
JVASP-103127	AllnSb ₂	115	<i>P-4m2</i>	0.242
JVASP-104	TiO ₂	141	<i>I4₁/amd</i>	2.023
JVASP-104764	Al ₃ GaN ₄	6	<i>Pm</i>	3.505
JVASP-105410	SiGe	216	<i>F-43m</i>	0.694
JVASP-10591	ZnS	186	<i>P6₃mc</i>	2.102
JVASP-106363	InGaCu ₂ Se ₄	82	<i>I-4</i>	0.022
JVASP-106686	ZnHgTe ₂	115	<i>P-4m2</i>	0
JVASP-1067	Bi ₂ Se ₃	166	<i>R-3m</i>	0.319
JVASP-107	SiC	186	<i>P6₃mc</i>	2.495
JVASP-10703	Cd ₃ As ₂	224	<i>Pn-3m</i>	0
JVASP-108770	InGaSb ₂	115	<i>P-4m2</i>	0
JVASP-110	BaTiO ₃	99	<i>P4mm</i>	1.749
JVASP-110231	InGaN ₂	156	<i>P3m1</i>	0.217
JVASP-1103	TePb	225	<i>Fm-3m</i>	1.119
JVASP-1109	SnS	62	<i>Pnma</i>	1.018
JVASP-111005	SnTe ₂ Pb	166	<i>R-3m</i>	0.488
JVASP-1112	PbS	225	<i>Fm-3m</i>	0.564
JVASP-1115	PbSe	225	<i>Fm-3m</i>	0.513
JVASP-113	ZrO ₂	14	<i>P2₁/c</i>	3.622
JVASP-1174	GaAs	216	<i>F-43m</i>	0.085
JVASP-1177	GaSb	216	<i>F-43m</i>	0
JVASP-1180	InN	186	<i>P6₃mc</i>	0
JVASP-1183	InP	216	<i>F-43m</i>	0.331
JVASP-1186	InAs	216	<i>F-43m</i>	0
JVASP-1189	InSb	216	<i>F-43m</i>	0
JVASP-1192	CdSe	216	<i>F-43m</i>	0.455
JVASP-1195	ZnO	186	<i>P6₃mc</i>	0.965
JVASP-1198	ZnTe	216	<i>F-43m</i>	1.057
JVASP-1201	CuCl	216	<i>F-43m</i>	0.729
JVASP-1216	Cu ₂ O	224	<i>Pn-3m</i>	0.644
JVASP-1222	UO ₂	225	<i>Fm-3m</i>	0
JVASP-1240	LiNbO ₃	161	<i>R3c</i>	3.339
JVASP-131	SnS ₂	164	<i>P-3m1</i>	1.224
JVASP-1312	BP	216	<i>F-43m</i>	1.515
JVASP-1327	AlP	216	<i>F-43m</i>	1.794
JVASP-133719	BAAs	216	<i>F-43m</i>	1.296
JVASP-1372	AlAs	216	<i>F-43m</i>	1.681
JVASP-1408	AlSb	216	<i>F-43m</i>	1.322
JVASP-14616	Li	229	<i>Im-3m</i>	0
JVASP-14968	TiSi ₂	70	<i>Fddd</i>	0
JVASP-14970	Si ₂ Mo	139	<i>I4/mmm</i>	0
JVASP-149871	GaAgS ₂	122	<i>I-42d</i>	0.89
JVASP-149906	ZnCdTe ₂	122	<i>I-42d</i>	0.68
JVASP-149916	SnTe	225	<i>Fm-3m</i>	0.479
JVASP-18983	TiO ₂	61	<i>Pbca</i>	2.254

Table S2: A detailed description of the materials in the test set (part two), including JARVIS-ID, space group number and symbol and band gap (vdW-DF-optB88).

JID	Formula	SPG Number	SPG Symbol	optb88vdw Band Gap (eV)
JVASP-1915	InSe	160	<i>R3m</i>	0.174
JVASP-19780	Si ₂ W	139	<i>I4/mmm</i>	0
JVASP-20092	CdO	225	<i>Fm-3m</i>	0
JVASP-21211	Se	152	<i>P3₁₂₁</i>	0.898
JVASP-22694	NiO	225	<i>Fm-3m</i>	0
JVASP-23	CdTe	216	<i>F-43m</i>	0.498
JVASP-2376	ZnSiP ₂	122	<i>I-42d</i>	1.428
JVASP-25	Bi ₂ Te ₃	166	<i>R-3m</i>	0.351
JVASP-29539	PbI ₂	186	<i>P6₃mc</i>	2.259
JVASP-30	GaN	186	<i>P6₃mc</i>	1.943
JVASP-32	Al ₂ O ₃	167	<i>R-3c</i>	6.43
JVASP-34249	HfO ₂	225	<i>Fm-3m</i>	4.037
JVASP-34674	SiO ₂	20	<i>C222₁</i>	5.673
JVASP-3510	BiI ₃	148	<i>R-3</i>	2.365
JVASP-36018	GeC	216	<i>F-43m</i>	1.927
JVASP-36408	SnC	216	<i>F-43m</i>	0.748
JVASP-36873	BSb	216	<i>F-43m</i>	0.945
JVASP-39	AlN	186	<i>P6₃mc</i>	4.474
JVASP-41	SiO ₂	154	<i>P3₂₂₁</i>	5.986
JVASP-4282	CrBr ₃	148	<i>R-3</i>	1.299
JVASP-43367	HfO ₂	61	<i>Pbca</i>	4.033
JVASP-5224	HgI ₂	137	<i>P4₂/nmc</i>	0.969
JVASP-54	MoS ₂	194	<i>P6₃/mmc</i>	0.922
JVASP-58349	SiO ₂	152	<i>P3₁₂₁</i>	5.985
JVASP-62940	BN	194	<i>P6₃/mmc</i>	4.46
JVASP-7836	BN	216	<i>F-43m</i>	4.813
JVASP-79522	CuO	131	<i>P4₂/mmc</i>	0
JVASP-8003	CdS	216	<i>F-43m</i>	0.993
JVASP-802	Hf	194	<i>P6₃/mmc</i>	0
JVASP-8082	SrTiO ₃	221	<i>Pm-3m</i>	1.814
JVASP-8118	SiC	186	<i>P6₃mc</i>	2.618
JVASP-813	Ag	225	<i>Fm-3m</i>	0
JVASP-8158	SiC	216	<i>F-43m</i>	1.62
JVASP-816	Al	225	<i>Fm-3m</i>	0
JVASP-8184	GaP	186	<i>P6₃mc</i>	1.263
JVASP-825	Au	225	<i>Fm-3m</i>	0
JVASP-85416	Ag ₂ S	14	<i>P2₁/c</i>	1.11
JVASP-85478	Cu ₂ S	96	<i>P4₃₂/12</i>	0.59
JVASP-8554	InCuSe ₂	122	<i>I-42d</i>	0.006
JVASP-8559	TlBr	221	<i>Pm-3m</i>	2.023
JVASP-861	Cr	229	<i>Im-3m</i>	0
JVASP-867	Cu	225	<i>Fm-3m</i>	0
JVASP-890	Ge	227	<i>Fd-3m</i>	0
JVASP-90668	ZnCu ₂ SnS ₄	82	<i>I-4</i>	0.115
JVASP-91	C	227	<i>Fd-3m</i>	4.457
JVASP-9117	FeS ₂	205	<i>Pa-3</i>	0.433
JVASP-9147	HfO ₂	14	<i>P2₁/c</i>	4.123
JVASP-9166	B ₆ As	166	<i>R-3m</i>	2.739
JVASP-943	Ni	225	<i>Fm-3m</i>	0
JVASP-96	ZnSe	216	<i>F-43m</i>	1.224
JVASP-963	Pd	225	<i>Fm-3m</i>	0
JVASP-972	Pt	225	<i>Fm-3m</i>	0
JVASP-99732	CdHg ₃ Te ₄	215	<i>P-43m</i>	0

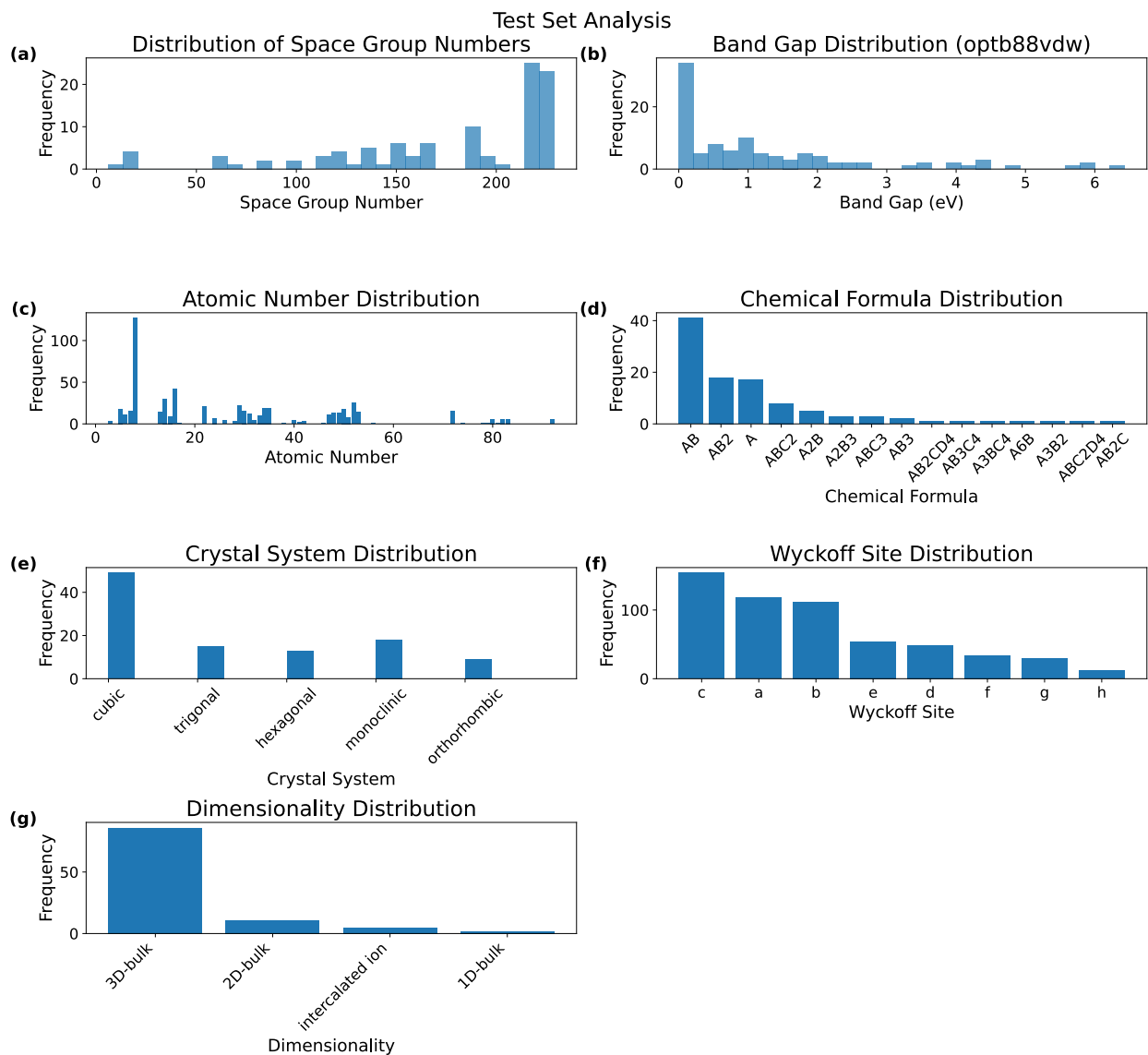


Fig. S1: The data distribution of the 104 materials in the test set for a) space group number, b) band gap (vdW-DF-optB88), c) atomic number, d) chemical formula, e) crystal system, f) Wyckoff site, g) dimensionality.